Oxidation Studies of Cu12Sb3.9Bi0.1S10Se3 Tetrahedrite

António Gonçalves, Elsa Lopes, Maria Montemor, Judith Monnier, Bertrand Lenoir

Oxidation Studies of the $Cu_{12}Sb_{3.9}Bi_{0.1}S_{10}Se_3$ Tetrahedrite

António P. Gonçalves,[1,*] Elsa B. Lopes,[1] Maria F. Montemor,[2] Judith Monnier,[3] Bertrand Lenoir[4]

[1] C[2]TN, Instituto Superior Técnico, Universidade de Lisboa, Estrada Nacional 10, 2695-066 Bobadela LRS, Portugal

[2] CQE, DEQ, Instituto Superior Técnico, Universidade de Lisboa, Av. Rovisco Pais 1049-001 Lisboa

[3] Université Paris Est, ICMPE (UMR 7182), CNRS, UPEC, F- 94320 Thiais, France

[3] Université de Lorraine, Institut Jean Lamour (UMR 7198) CNRS-UL, Parc de Saurupt, CS 50840, 54011 Nancy, France

Corresponding author:

A.P. Gonçalves

Address: C[2]TN, Instituto Superior Técnico, Universidade de Lisboa

Centro de Ciências e Tecnologias Nucleares, Departamento de Engenharia e Ciências Nucleares, Estrada Nacional 10, 2695-066 Bobadela LRS, Portugal

Email: apg@ctn.tecnico.ulisboa.pt ***Tel***.: +351 219946182

Abstract

Tetrahedrites are widespread minerals with $Cu_{10}M_2Sb_4S_{13}$ (*M* = Cu, Mn, Fe, Co, Ni, Zn) general formula, whose thermoelectric properties can be tuned through proper doping and reach *zT* values as high as 1, being considered promising low-cost materials for thermoelectrics. However, for their practical applications in thermoelectric devices it is necessary to establish their ability to operate for long periods under the working temperatures and atmospheres. Here we present the oxidation studies in air of the $Cu_{12}Sb_{3.9}Bi_{0.1}S_{10}Se_3$ tetrahedrite at four different temperatures, between 230ºC and 375ºC, together with preliminary corrosion studies in aggressive NaCl electrolytes. Surface oxidation already occurs at the lower studied temperatures, but a strong decrease of the oxidation rate is observed in materials treated at medium temperatures (275ºC), where a continuous surface layer of $Cu_{2-x}S$ forms, pointing to the protector effect of this layer that could be used in devices at those temperatures. For the materials treated at higher temperatures (350ºC and 375ºC) no tetrahedrite phases are seen after 1500 h, which can be related to the (Tetrahedrite + Chalcostibite + Antimony → Skinnerite) reaction that occurs above 280ºC. Corrosion studies indicate that increasing the oxidation temperature leads unfortunately to a decrease of the corrosion resistance of tetrahedrite-based phases.

Keywords

Tetrahedrite; low-cost thermoelectric materials; oxidation; thermal stability.

1. **Introduction**

Energy is deeply involved in the social, economic and environmental dimensions of human development. However, and albeit its importance, more than half of the energy produced by man is lost, either during generation, transport or consumption [1]. The lost energy is mainly vanished as waste heat, which leads to an enormous interest in the use of clean technologies for its recovery. Thermoelectric materials can be employed in devices that directly convert heat into electricity (via the Seebeck effect) and, vice versa, heating or cooling through the passage of an electrical current (via the Peltier effect). Moreover, thermoelectric devices have no moving parts, work in silence, are reliable and do not release any gases or generate chemical waste during operation. As a result, thermoelectric technology is seen as having great potential to contribute for the recovery of waste heat, increasing the energy efficiency, reducing the greenhouse gas emissions and promoting a more sustainable world.

The performance of a thermoelectric material can be estimated from its dimensionless thermoelectric figure of merit, zT [2], which depends only on the material properties, relating the Seebeck coefficient (α), electrical conductivity (σ) and thermal conductivity (λ) at the absolute temperature (T), and it is expressed by equation (1)

$$zT = \sigma \alpha^2 T / \lambda \quad (1)$$

The figure of merit allows an extensive and systematic classification of materials for thermoelectrics, and it is desirable to have the highest achievable value over the wider temperature range possible in order to optimize the power generating efficiency of the thermoelectric device [3]. Actual commercial equipments, which are composed of materials with $zT \approx 1$, are mostly based on rare or toxic raw materials, e.g., Te, Bi and Pb. Therefore, an increasing focus on the development of new thermoelectric materials made of non-toxic earth-abundant elements was lately seen. In this

context, tetrahedrite-based materials have recently attracted great attention, as they present figures of merit close to unity at medium temperatures (230ºC-430ºC) [4,5,6,7,8,9,10,11,12,13,14,15,16,17,18]. Tetrahedrites are copper sulfosalt minerals widely found all around the wourld with $Cu_{10}M_2Sb_4S_{13}$ (*M* = Cu, Mn, Fe, Co, Ni, Zn) general formula and cubic (S.G. I-43m) $Cu_{12}Sb_4S_{13}$-type crystal structure [19,20,21]. In the $Cu_{12}Sb_4S_{13}$-type structure, copper is located at two different crystallographic sites, tetrahedral 12*d* and trigonal planar 12*e*, the last one (12*e*) being inside a triangle of three sulfur atoms that allows the vibration of the central atom perpendicular to the triangle with large atomic displacement parameter. This vibration is considered one of the main reasons for the good thermoelectric performance observed in these materials, as it promotes large phonon-phonon scattering that leads to low thermal conductivities [5,22]. The highest figures of merit are reached after tuning the carrier concentration (through proper doping with transition metals or tellurium [4,5,7-13,15,16]) or by changing the valence band configuration (via the substitution of selenium for sulfur or bismuth for antimony [14,18]). However, to consider the use of tetrahedrite-based materials in practical devices, it is not only necessary to have good thermoelectric properties, but also to prove their ability to operate for long periods under the working temperatures and atmospheres. The oxidation and/or corrosion usually promote the degradation of intrinsic properties, such as thermal and electrical transport ones, making the materials unsuitable for applications. Vacuum preservation or a protective coating/environment are possibilities that, if achievable, must be avoided due to their cost and the technical problems for keeping them at the working temperatures. However, up to the author's best knowledge, no oxidation and corrosion studies have been reported until now for tetrahedrite-based materials. It is therefore important to study the oxidation behavior of these materials in the whole temperature range they may exist, which means up to their melting and/or sublimation.

Here we present the oxidation study of the $Cu_{12}Sb_{3.9}Bi_{0.1}S_{10}Se_3$ tetrahedrite at four different temperatures, between 230ºC and 375ºC, in air, for 1500 h. This peculiar composition, with Bi and

Se, was chosen regarding the difficulties to prepare pure tetrahedrite $Cu_{12}Sb_4S_{13}$ samples (due to the exsolution problem and presence of secondary phases, even after a long-term annealing) and the reported thermoelectric properties of substituted materials. In a previous work, we studied the influence of Bi, Se and Ni on the tetrahedrite stability, and concluded that substitution with Se enables a maximization of the percentage of tetrahedrite phase formed [23]. Moreover, Bi and Se, albeit only inducing changes in the valence band configuration, have been reported as giving tetrahedrite-based materials with good thermoelectric performance [14,18]. Preliminary corrosion studies assessed by Electrochemical Impedance Spectroscopy (EIS) in aggressive NaCl electrolytes are also shown. Eventually, the $Cu_{12}Sb_{3.9}Bi_{0.1}S_{10}Se_3$ composition would be a good starting material for further studying the substitutions with transition metals. To carry out this work the materials subjected to the different conditions were characterized by X-ray diffraction (XRD), differential scanning calorimetry (DSC), thermogravimetry (TG), optical microscopy (OM) and scanning electron microscopy (SEM), complemented with energy-dispersive spectroscopy (EDS).

2. Material and methods

A polycrystalline sample with $Cu_{12}Sb_{3.9}Bi_{0.1}S_{10}Se_3$ nominal composition and a mass of ~3.5 g was prepared by reacting the stoichiometric amount of the elements (Cu, ≥99.999%, Sigma-Aldrich; Sb, 99.999%, Ventron; Bi, 99.997%, Alfa Aesar; S, 99.9%, Alfa Aeser; Se, 99.99+%, Sigma-Aldrich) inside a quartz ampoule of 10 mm outer diameter and 1 mm wall thickness sealed under vacuum. The temperature of the mixture was raised from room temperature to 950ºC with an average heating speed of 3ºC/min, kept at that temperature for 60 min and slowly cooled (3ºC/min) down to 100ºC, before being removed from the furnace.

The as-prepared sample was hand-ground before being sintered. Spark Plasma Sintering (SPS) was realized with the Dr. Sinter 505 Syntex, the set-up belonging to the “Plate-forme de

Frittage Ile de France" (Thiais, France). The powder was introduced in a 8 mm diameter graphite die. To densify we used a dwell time parameter of 5 min at 360°C and under the pressure of 80MPa.

A TA Instruments Q100 differential scanning calorimeter was used on the thermodynamic characterization of the SPS material. The DSC measurements were made in a powdered piece of the SPS pellet, with a mass of ~10 mg, under an argon flux of 50 cm^3/min. The temperature ranged from room temperature up to 600ºC, with a heating speed of 10ºC/min. The inflection points were used to characterize the phenomenon temperatures. TG analysis of the SPS material was performed using a TA Instruments– 951 Thermogravimetric Analyser for continuous oxidation studies. The TG measurements were made with a SPS sample with triangular prism shape having ~31 mg weight, from room temperature up to 700 ºC, a heating rate of 10 ºC/min and under air atmosphere with a flux of 60 cm^3/min.

Isothermal oxidation studies for the $Cu_{12}Sb_{3.9}Bi_{0.1}S_{10}Se_3$ tetrahedrite were conducted at 230ºC, 275ºC, 350ºC and 375ºC for 1500 h under ambient laboratory air without flux. The pellet obtained from the SPS procedure was cut in triangular prism shaped pieces. All surfaces were polished with SiC abrasive papers (1000 and 2500 mesh) and cleaned with acetone. The dimensions of the prisms were measured with the help of a caliper, typically resulting in 30-40 mm^2 total surface areas, which were used in the calculations. The triangular prism shaped samples were directly put inside resistive tube furnaces pre-set at the desired temperatures. Alumina crucibles were used as sample holders and k-type thermocouples were placed close to the samples to control the temperatures (±5ºC temperature stability). The samples were periodically removed from the furnaces and their mass was carefully measured three times before and after the tests, in order to determine the changes. Normalized weight changes were calculated in the unit of mg/mm^2 by dividing the weight change values of the heat treated samples to their total surface areas.

XRD was used to characterize the phases that exist in the original material (before the oxidation studies) and in each of the treated samples after the total oxidation treatment, at two

different regions: i) at the oxidized surfaces; and ii) in the interior of the samples. For the original (non-oxidized) material a representative part of the SPS pellet was manually powdered and studied by powder XRD. The oxide phases formed during the isothermal treatments were characterized by measuring the X-ray diffractograms on the surfaces of the samples treated during 1500 h. Finally, to characterize the interior of the samples after the oxidation process a small portion was removed from each piece after the 1500 h treatment, was reduced to powder and was used in the XRD studies. Low-noise Si single crystal XRD sample holders were employed in a PANalytical X'Pert Pro powder diffractometer (Cu Kα-radiation) with Bragg-Brentano geometry. Step-scanning mode XRD patterns were taken in the 15–65º 2θ region with the $\theta/2\theta$ configuration, a step scan of 0.04º and a counting time per step of 4 s. The theoretical powder patterns were calculated with the help of the Powder-Cell package [24]. The lattice parameters and unit cell volumes were obtained by least-squares fitting using the UnitCell program [25].

The surface of the samples was observed by OM, using a Olympus BX60M microscope. SEM was used to characterize the microstructure of the oxidized samples. The SEM observations were made on polished cross section using a JEOL JSM-7001F field emission gun scattering electron microscope, equipped for EDS with a light element detector, which was used for the chemical quantification of the elements in the phases.

For assessing the corrosion resistance four different type of samples were tested: the reference (as prepared) sample and samples oxidized at 230ºC, 275ºC and 375ºC in air for 2 h. The electrochemical impedance spectroscopy (EIS) measurements were performed at room temperature over time on the tetrahedrite coupons mounted in epoxy resin and immersed in 0.05M NaCl using a Gamry potentiostat. The spectra were collected for immersion times of 2 h and 60 h in a frequency range from 1×10^{4} down to 1×10^{-2} Hz. All the spectra were recorded at open circuit potential while applying a 10 mV sinusoidal perturbation. A conventional three-electrode cell was used, consisting of a saturated calomel reference electrode, a platinum coiled wire as a counter electrode and the

tetrahedrite as working electrode. The area of the working electrode was approximately 3.1 cm^2. The cell was placed in a Faraday cage to avoid external interferences and stray currents.

3. Results and discussion

The X-ray diffractogram of the SPS original material is presented in Figure 1. The SPS sample is mainly constituted by tetrahedrite and small amounts of skinnerite (Cu_3SbS_3) and chalcostibite ($CuSbS_2$). The DSC characterization of this sample under argon atmosphere shows the existence of an anomaly at 280(5)ºC followed by several endothermic peaks between 425ºC and 540ºC, before the final melting at 550(5)ºC (Figure 2). Similar anomalies were previously observed in DSC measurements of tetrahedrites, being ascribed to the Class III reaction (Tetrahedrite + Chalcostibite + Antimony → Skinnerite) [23] (the minor amounts of Sb involved here did not allow detection by XRD), while the negative peeks are related to other reactions involving the tetrahedrite phase [26,27]. The final melting temperature is significantly lower than the one of the 12Cu:4Sb:13S material composition (unsubstituted tetrahedrite), which is 605ºC and corresponds to the skinnerite congruent melting temperature [26]. A previous study on the effect of elements in the tetrahedrite formation showed that the substitution of selenium for sulfur strongly decreases the Class III reaction and final melting temperatures [23], being in agreement with the present data.

TG results are plotted in Figure 3. The weight of the sample increases above 320(5)ºC, which evidences quick oxidation reactions. However, this increase occurs only up to 400(5)ºC and afterwards a weight loss is observed, indicating a predominance of evaporation/sublimation of some of the components (S and Se), albeit oxidation is expected to occur continuously. Moreover, this weight decrease is not continuous, having two steps, with the derivative of the TG curve (insert in Figure 3) showing negative peeks between 460(5)ºC-500(5)ºC and 580(5)ºC-630(5)ºC, with minima

at 480(2)ºC and 605(2)ºC, respectively. It must be noticed that the first step corresponds to 3.3(1)% of the initial weight, while the second corresponds to 11.0(1)% and none of these values or their sum is consistent just with the S or Se weight percentage in the sample (S: 17.6 w.%; Se: 13.1 w.%). Weight losses above 450ºC were previously observed in TG measurements performed under nitrogen atmosphere on $Cu_{12}Sb_4S_{13}$ tetrahedrites [28], being attributed to S volatilization. In the present case the situation is more complex, reflecting not only the presence of oxygen in the atmosphere (and the corresponding oxidation of the sample), but also of sulfur and selenium in the sample and their occupation at the different crystallographic positions. Besides, in the temperature range analyzed several solid state reactions and melting occur, with kinetic effects also playing a role [28].

Figure 4 shows the normalized weight change of the $Cu_{12}Sb_{3.9}Bi_{0.1}S_{10}Se_3$ tetrahedrite as a function of time, at 230ºC, 275ºC, 350ºC and 375ºC under air atmosphere. Two of the temperatures were chosen to be below 320ºC, while the other two were chosen between 320ºC and 400ºC. These limit temperatures were selected based on the TG results: above 320ºC a weight gain is observed in the measurements, while above 400ºC a weight loss starts to be seen. Therefore, one could expect that no oxidation or only limited oxidation would exist up to 320ºC and that between this temperature and 400ºC the tetrahedrite quickly oxidizes.

For the treatments made at 230ºC and 275ºC a small but continuous weight gain is observed. Albeit not evident in the TG measurements (most possibly due to its sensitivity, the low reaction kinetics and the small values involved), these results clearly show that oxidation already exists at those temperatures, indicating an important role of kinetics. Actually, the oxidation kinetics depends on variables like the type of material, surface preparation, oxygen pressure, oxygen flux or temperature. In the present study the isothermal oxidation kinetics is analyzed below for the different temperatures, the other factors being kept constant.

In the case of the materials treated at 230ºC it is first observed a weight gain, faster at the beginning and diminishing with time (Figure 4a). This points to an oxidation rate faster at the start, decreasing with the increasing of time, and a negligible sublimation/evaporation processes. Several rate laws, like linear, parabolic, logarithmic and combinations of them, are commonly considered in the oxidation of materials, their functionality giving information on how the oxide grows [29]. The weight gain at 230ºC can be well adjusted by the logarithmic curve [30]

$$\Delta m/S = k \log(t + t_0) + A \quad (2)$$

in all the time-scale (Figure 4b), where S represents the surface area, $\Delta m/S$ is the normalized weight gain, k is the rate constant, t and t_0 are the time and initial time, and A is a constant. At 230ºC the least squares fitting gives k, t_0 and A values of $7.9(3)*10^{-3}$, 1.6(6) and $-2(2)*10^{-3}$, respectively, with a R^2 of 0.96. Logarithmic reaction rates are frequently observed in low temperatures oxidations, when a thin film of oxide is formed, the rate-limiting mechanisms usually being the ionic and/or electron transport processes through the oxide film [29, 30].

At 275ºC the faster weight gain at the start, diminishing with time, is also observed, again pointing to the predominance of the oxidation reactions at this temperature. However, in this case the weight gain at the beginning is faster and decreases quickly with time than the one at 230ºC (Figure 4a). Moreover, the final weight gain (after the 1500 h) at 275ºC is only 42% of that at 230ºC (Figure 4b). At this last temperature the weight gain versus time data could not be acceptably adjusted just by a logarithmic curve. Therefore, to analyze the oxidation kinetics at 275ºC the fit of the normalized weight gain data was first made using the following equation [31]

$$\Delta m/S = K\, t^{1/n} \quad (3)$$

where K is the rate constant and n is the reaction kinetics index. It must be noticed that in most of the cases n takes the values 1, 2 or 3, which corresponds to linear, parabolic or cubic reaction rates, respectively. A linear reaction kinetics indicates that an oxide barrier never protects the surface and that the oxidation remains constant with time. In the parabolic kinetics the oxidation process is rate-limited by the diffusion of the ions through a compact layer of oxide. Higher reaction kinetics indexes (including the cubic one) are usually considered intermediate stages between the logarithmic and parabolic kinetics [29]. In the case of samples treated at 275ºC the best fitting was obtained for $K = 5.3*10^{-16}$ and $n \approx 7$, which points to an intermediate stage and indicates the formation at this temperature of a complex layer barrier that strongly interferes with the diffusion of ions [29]. According to this model, the kinetic curves can be decomposed into a parabolic term and a logarithmic term, leading to

$$\Delta m/S = a\, t^{1/2} + b\, (\log(t + t_0) + A) \qquad (4)$$

Using this last formula, the least squares fitting of the 275ºC data gives a, b, t_0 and A values of $3.4(2)*10^{-4}$, $4.0(2)*10^{-4}$, 0.0(1) and 25.1(3), respectively, with a R^2 of 0.92, confirming the intermediate stage of oxidation kinetics at this temperature.

The 350ºC and 375ºC isothermals show a distinct behavior from that observed before for the two previous temperatures. A weight decrease is first seen, contrasting with the TG results and indicating that, in parallel with the oxidation, a slow sublimation and/or evaporation exists at those temperatures and that it prevails at the beginning. This weight decrease is followed by a weight gain, whose rate diminishes with time, pointing to the predominance of oxidation processes after some hours. The complexity of the processes involved, with simultaneous oxidation and sublimation/evaporation of components, did not allow the satisfactory adjustment of any rate law and the obtaining of constants with physical meaning. However, it should be noticed that at higher

temperatures all processes are quicker (as expected) and that in both cases the final weight change converges to a similar value, pointing to the formation of identical final materials.

Representative cross-sectional (internal) microstructures of the $Cu_{12}Sb_{3.9}Bi_{0.1}S_{10}Se_3$ material oxidized at 230ºC, 275ºC, 350ºC and 375ºC for 1500 h are presented in Figure 5. Optical micrographs of the surfaces of the samples are shown in Figure 6. X-ray diffractograms of the interior and surface of the same materials, together with the simulations for tetrahedrite ($Cu_{12}Sb_4S_{14}$), famatinite (Cu_3SbS_4), digenite ($Cu_{1.8}S$), berzelianite (Cu_2Se), chalcostibite ($CuSbS_2$), skinnerite (Cu_3SbS_3), copper sulfate ($CuSO_4$), copper-antimony trirutile-type oxide ($CuSb_2O_6$) and antimony tetroxide (Sb_2O_4) crystal structures, are presented in Figure 7. Table I summarizes the average EDS analysis results for the phases in the $Cu_{12}Sb_{3.9}Bi_{0.1}S_{10}Se_3$ oxidized samples.

The interior of the material oxidized at 230ºC is mainly constituted by a grey phase with a composition compatible with tetrahedrite (Table I). Two other minor phases, a dark grey and a white one, are also observed, the image analysis indicating that they represent 35 vol.% and 3 vol.% of the sample, respectively. The EDS analysis of the white phase matches well with the chalcostibite ($CuSbS_2$) composition, while in the case of the dark grey phase it was not possible to find any reported compound compatible with the EDS results. XRD data confirm tetrahedrite as the major phase, the remaining peaks belonging to a famatinite-type structure (chalcostibite is not observed, probably due to its small volume percentage). In famatinite the ratio between antimony and sulfur is 0.25, which fits well with the EDS analysis (the atomic ratio between antimony and (sulfur + selenium) is 0.30(6)), but the copper atomic percentage is too high in the dark grey phase and no oxygen should be present. However, three aspects must be noticed, i) numerous pores occur in this phase, ii) there is always a contact between the phase (and, consequently, the pores) and the surface of the sample and iii) a great oscillation in the copper and oxygen atomic percentage between each individual analysis is observed. Therefore, most probably a small layer of copper oxides have been formed at the surface of the pores, which could explain the observed oscillations

in the content of these two elements. Moreover, this quantity is small and the contrast is poor (making it very difficult to observe by SEM), the small diffraction peaks of the possible copper oxides are located just at the same position of tetrahedrite ones (making it very hard to identify them) and contamination from the neighbor phases exist. The surface of the sample treated at 230ºC shows the presence of a porous external layer full of cracks (Figure 6 and insert in Figure 5 a)), which was identified from EDS analysis and XRD data as being mainly formed by copper sulfate and berzelianite.

The sample oxidized at 275ºC has an interior similar to that of the sample treated at 230ºC, also with three phases, a grey, a dark grey and a white one, but with much less porosity (Figure 5 b)). In this case, the EDS analysis clearly indicates that the grey phase consists of tetrahedrite, the dark grey is famatinite (Cu_3SbS_4) and the white is chalcostibite ($CuSbS_2$), which is also confirmed by the XRD data. Here, image analysis points to relative volume percentages of 45 vol.%, 50 vol.% and 5 vol.% for tetrahedrite, famatinite and chalcostibite, respectively, indicating that tetrahedrite had some degradation during the treatment at this temperature and that was an enrichment of S+Se in the interior. The surface of the sample is covered by a film of oxides that were identified as $CuSO_4$ and $CuSb_2O_6$, with also small quantities of Cu_2Se, pointing to some migration of copper from the interior to the surface. This film is denser and has less cracks than the one observed at 230ºC. Contrasting with the sample treated at 230ºC, below this coating a continuous layer of $Cu_{2-x}S$ exists. The presence of the $Cu_{2-x}S$ layer is most probably the reason for the lower weight change observed here (when compared with the sample treated at 230ºC), as it seems to act as a barrier for the diffusion of ions, reducing the oxidation.

Both materials oxidized at 350ºC and 375ºC have a microstructure very different from the lower temperature ones (Figures 5 c) and d)). No sign of a tetrahedrite phase is present in any of them, the EDS analysis and powder XRD pointing to digenite ($Cu_{1.8}S$, dark grey) and skinnerite (Cu_3SbS_3, grey) as the main interior constituents (Figure 7a).

The surface of the material treated at 350ºC is inhomogeneous, with some parts optically similar to the 275ºC and others analogous to the 375ºC materials (Figure 6). As a result, no X-ray diffractograms were collected in the surface of this sample. The material treated at 375ºC is externally mainly covered by an antimony oxide layer (Sb_2O_4, white), which is making nodules in the interior too. Copper antimony oxide ($CuSb_2O_6$) and skinnerite layers are also observed. The external oxide layers are full of pores, while skinnerite is continuous and homogeneous. The surface of the material oxidized at 375ºC is extremely damaged, full of cracks and large pores, easily letting oxygen diffuse. On the contrary, the continuous skinnerite layer can act as an effective barrier for the diffusion of oxygen, being most probably the reason for the low weight increase at this temperature.

The total impedance values obtained from the EIS measurements can be correlated to the corrosion resistance of the material. Impedance Bode plots obtained for the reference sample and for the 230ºC, 275ºC and 375ºC oxidized samples at 2 and 60 h immersion times in a 0.05M NaCl solution are presented in Figure 8 a), b) c) and d). At short immersion times the EIS spectra allowed to discriminate two distinct behaviors that agree with the observed differences in the microstructure and phases described above. The highest impedance values, accompanied by a more negative phase angle, account for increased corrosion resistance, and were observed for the non-oxidized sample, closely followed by the sample oxidized at 375ºC. The samples oxidized at lower temperatures (230ºC and 275ºC), which have similar microstructures and phases, showed lower impedance values and decreased phase angle, shifted to lower frequencies. The increase of the phase angle at low frequencies may account for the presence of mass controlled corrosion processes. These results clearly point out that the increasing oxidation temperatures leads to decreased corrosion resistance of samples with tetrahedrite-based phases when aggressive species are present in the medium. The reference sample revealed a monotonous behavior with time, with the overall impedance values slightly decreasing from approximately $9x10^4$ Ohm.cm^2 (2 h) to $5x10^4$ Ohm.cm^2 (60 h) (Figure 8

e)). For the other two samples containing tetrahedrite-based phases (230ºC and 275ºC) the behavior was characterized by a monotonous decrease of the impedance with time, from values around $2x10^3$ Ohm.cm^2 (2 h) to values close to $1x10^3$ Ohm.cm^2 (after 60 h of immersion) (Figure 8 e)). The sample oxidized at 375ºC revealed a different behavior, a slight increase of the corrosion resistance, with the overall impedance values being increased from $4x10^4$ Ohm.cm^2 up to $2x10^5$ Ohm.cm^2 (Figure 8 e)). Overall, these results demonstrate that the reference sample is the most resistant to corrosion and that the samples oxidized at 375ºC (without tetrahedrite) possess higher corrosion resistance over time when compared with the other samples. Since the external oxide is porous it may be expected that the continuous and homogeneous skinnerite layer is responsible for the delay of the corrosion attack in the samples oxidized at 375ºC. Eventually the slight increase can be due to sealing of the outer pores by the corrosion products.

Conclusions

The present work shows that the $Cu_{12}Sb_{3.9}Bi_{0.1}S_{10}Se_3$ tetrahedrite slowly oxidizes at temperatures as low as 230ºC. The analysis of the oxidation kinetics indicates that at this temperature the rate-limiting mechanism is the ionic and/or electron transport processes through an oxide film. At slightly higher temperatures (275ºC) the curve adjustment of the weight gains points to the formation of a complex layer barrier that strongly interferes with the diffusion of ions. The microstructural analysis agrees with such observations, showing the formation of a layer of surface oxides at 230ºC, while at 275ºC a continuous $Cu_{2-x}S$ surface barrier, which prevents the advance of oxidation, also exists. At higher temperatures (350ºC and 375ºC) no tetrahedrite-based phases are found in the samples after 1500 h. Here, competing oxidation and volatilization processes occur, together with the (Tetrahedrite + Chalcostibite + Antimony → Skinnerite) reaction that promotes the decomposition of tetrahedrite and happens above 280ºC. Corrosion studies indicate that

increasing oxidation temperature leads to decreased corrosion resistance on the samples containing tetrahedrite-based phases, when aggressive species are present in the medium.

In conclusion, it was shown that tetrahedrite-based phases oxidize at medium temperatures, but it is possible to decrease the oxidation rate to very low values through the formation of a $Cu_{2-x}S$ surface barrier. This points that sealing the leg-surface with $Cu_{2-x}S$ can protect it against oxidation up to temperatures above which volatilization is important and the Class III reaction (that promotes the skinnerite formation) occurs. However, to confirm this assumption further studies are needed. Moreover, the maximum temperatures should strongly depend on the materials composition, which must also be investigated.

Acknowledgments

This work was partially supported by the Portuguese Foundation for Science and Technology (FCT), Portugal, through the contracts UID/Multi/04349/2013, POCI-01-0145-FEDER-016674 and M-ERA-NET2/0010/2016. We would also like to acknowledge the support given by the French National Agency (ANR) in the frame of its program "PROGELEC" (Verre Thermo-Générateur "VTG").

Figure Captions

Figure 1. X-ray diffractogram of the SPS original $Cu_{12}Sb_{3.9}Bi_{0.1}S_{10}Se_3$ material.

Figure 2. DSC characterization of $Cu_{12}Sb_{3.9}Bi_{0.1}S_{10}Se_3$ material under argon atmosphere, from room temperature up to 600°C at 10ºC/min. Inset presents the enlarged region between 180ºC and 300ºC.

Figure 3. TG measurement of the $Cu_{12}Sb_{3.9}Bi_{0.1}S_{10}Se_3$ tetrahedrite, from room temperature up to 700 ºC at 10 ºC/min and under air atmosphere. Inset: derivative of the TG curve.

Figure 4. Normalized weight change of the $Cu_{12}Sb_{3.9}Bi_{0.1}S_{10}Se_3$ tetrahedrite as a function of time, at 230ºC, 275ºC, 350ºC and 375ºC under air atmosphere, between a) 0 h and 20 h and b) 0 h and 1500 h. Plain lines represent rate laws associated to oxidation kinetics at 230°C (logarithmic curve) and 275°C (intermediate stage). Dashed lines are only a guide to the eyes.

Figure 5. SEM cross-sectional microstructures of the $Cu_{12}Sb_{3.9}Bi_{0.1}S_{10}Se_3$ material oxidized at a) 230ºC, b) 275ºC, c) 350ºC and d) 375ºC for 1500 h. Inset shows the enlarged surface of the material oxidized at 230ºC.

Figure 6. Optical micrograph of the surface of the $Cu_{12}Sb_{3.9}Bi_{0.1}S_{10}Se_3$ material oxidized at a) 230ºC, b) 275ºC, c) 350ºC and d) 375ºC for 1500 h.

Figure 7. X-ray diffractograms of the (a) interior and (b) surface of the $Cu_{12}Sb_{3.9}Bi_{0.1}S_{10}Se_3$ material oxidized, together with the crystal structures simulations for tetrahedrite ($Cu_{12}Sb_4S_{13}$), famatinite (Cu_3SbS_4), digenite ($Cu_{1.8}S$), berzelianite (Cu_2Se), chalcostibite ($CuSbS_2$), skinnerite (Cu_3SbS_3), copper sulfate ($CuSO_4$), copper-antimony trirutile-type oxide ($CuSb_2O_6$) and antimony tetroxide (Sb_2O_4).

Figure 8. EIS spectra of the reference, 230ºC, 275ºC and 375ºC oxidized materials at a) and b) 2 h and c) and d) 60 h; e) impedance moduli at 1×10^{-2} Hz versus time.

References

[1] Library, L.L.N. U.S. Energy Flow. 2014 [cited 2015 25. October]; Available from: https://flowcharts.llnl.gov/.

[2] A.F. Ioffe, *Energetic basis of thermoelectrical cells from semiconductors*, Academy of Sciences of the USSR, Moscow **1950** (in Russian).

[3] C. Wood, *Rep. Prog. Phys*. **1988**, *51*, 459.

[4] X. Lu, D. T. Morelli, Y. Xia, F. Zhou, V. Ozolins, H. Chi, X. Zhou, C. Uher, *Adv. Energy Mater*. **2013**, *3*, 342.

[5] K. Suekuni, K. Tsuruta, M. Kunii, H. Nishiate, E. Nishibori, S. Maki, M. Ohta, A. Yamamoto, M. Koyano, *J. Appl. Phys*. **2013**, *113*, 043712.

[6] X. Lu, D. T. Morelli, *Phys. Chem. Chem. Phys*. **2013**, *15*, 5762.

[7] X. Lu, D. Morelli, *J. Electron. Mater*. **2014**, *43*, 1983.

[8] J. Heo, G. Laurita, S. Muir, M. A. Subramanian, D. A. Keszler, *Chem. Mater*. **2014**, *26*, 2047.

[9] R. Chetty, P. Kumar D. S., G. Rogl, P. Rogl, E. Bauer, H. Michor, S. Suwas, S. Puchegger, G. Giesterg, R. C. Mallik, *Phys. Chem. Chem. Phys*. **2015**, *17*, 1716.

[10] X. Lu, D. T. Morelli, Y. Xia, V. Ozolins, *Chem. Mater*. **2015**, *27*, 408.

[11] X. Lu, D. T. Morelli, *J. Electron. Mater*. **2014**, *43*, 1983.

[12] Y. Bouyrie, C. Candolfi, V. Ohorodniichuk, B. Malaman, A. Dauscher, J. Tobola, B. Lenoir, *J. Mater. Chem. C* **2015**, *3*, 10476.

[13] R. Chetty, A. Bali, M.H. Naik, G. Rogl, P. Rogl, M. Jain, S. Suwas, R. C. Mallik, *Acta Mater*. **2015**, *100*, 266.

[14] X. Lu, D. T. Morelli, Y. Wang, W. Lai, Y. Xia, V. Ozolins, *Chem. Mater*. **2016**, *28*, 1781.

[15] Y. Bouyrie, S. Sassi, C. Candolfi, J.-B. Vaney, A. Dauscher, B. Lenoir, *Dalton Trans*. **2016**, *45*, 7294.

[16] D. S. P. Kumar, R. Chetty, P. Rogl, G. Rogl, E. Bauer, P. Malar, R. C. Mallik, *Intermetallics* **2016**, *78*, 21.

[17] T. Barbier, S. Rollin-Martinet, P. Lemoine, F. Gascoin, A. Kaltzoglou, P. Vaqueiro, A. V. Powell, E. Guilmeau, *J. Am. Ceram. Soc*. **2016**, *99*, 51.

[18] D. S. P. Kumar, R. Chetty, O.E. Femi, K. Chattopadhyay, P. Malar, R.C. Mallik, *J. Electron. Mater*. **2017**, 1-7.

[19] L. Pauling, E. W. Neuman, *Z. Kristallogr*. **1934**, *88*, 54.

[20] B. J. Wuensch, *Science* **1963**, *141*, 804.

[21] B. J. Wuensch, *Z. Kristallogr*. **1964**, *119*, 437.

[22] W. Lai, Y. Wang, D. T. Morelli, X. Lu, *Adv. Funct. Mater*. **2015**, *25*, 3648.

[23] A. P. Gonçalves, E. B. Lopes, B. Villeroy, J. Monnier, C. Godart, B, Lenoir, *RSC Adv*. **2016**, *6*, 102359.

[24] G. Nolze, W. Kraus, Powder Cell for Windows (Version 2.3), Federal Institute for Materials Research and Testing, Berlin, Gremany, **1999**.

[25] T. J. B. Holland, S. A. T. Redfern, *Mineral. Mag*. **1997**, *61*, 65.

[26] B. J. Skinner, F. D. Luce, E. Makovicky, *Economic Geology* **1972**, *67*, 924.

[27] M. H. Braga, J. A. Ferreira, C. Lopes, L. F. Malheiros, *Materials Science Forum* **2008**, *587-588*, 435.

[28] T. Barbier, P. Lemoine, S. Gascoin, O. I. Lebedev, A. Kaltzoglou, P. Vaqueiro, A. V. Powell, R. I. Smith, E. Guilmeau, *J. Alloys Comp*. **2015**, *634*, 253

[29] A.S. Khanna, *Introduction to High Temperature Oxidation and Corrosion*, ASM International, Materials Park, OH, **2002**.

[30] *ASM Specialty Handbook: Heat-Resistant Materials*, (Ed: J.R. Davis), ASM International, **1997**.

[31] P. Kofstad, *High Temperature Corrosion*, Elsevier Applied Science, Essex, **1988**.

Figure 1

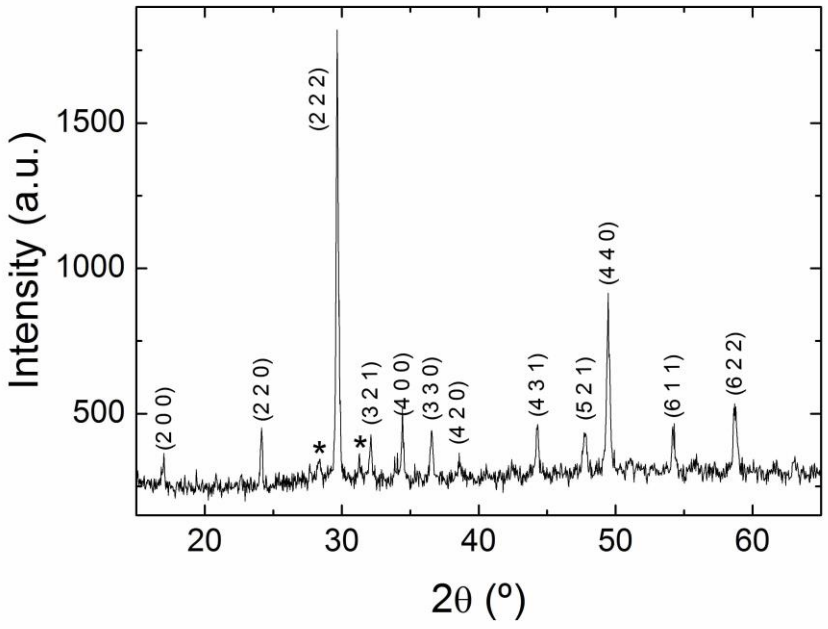

Figure 2

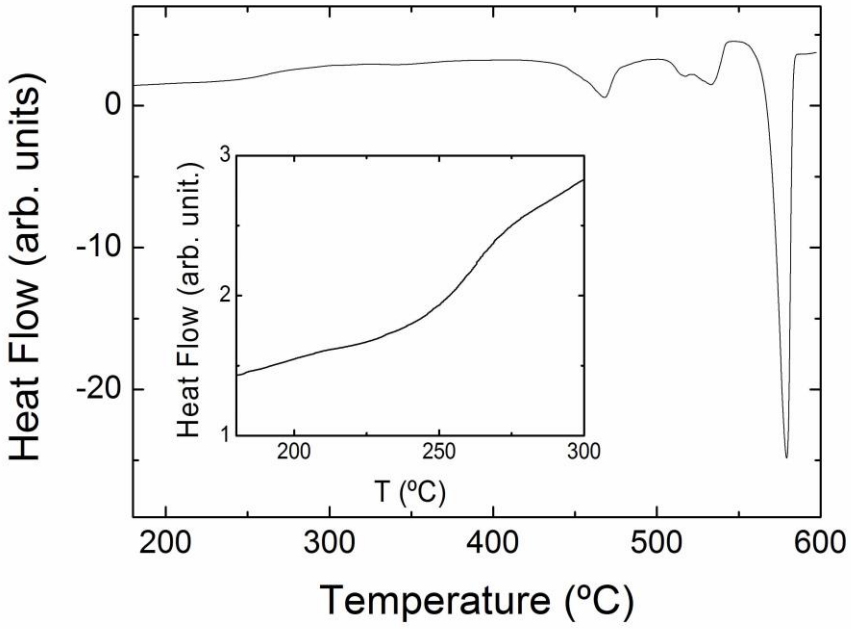

Figure 3

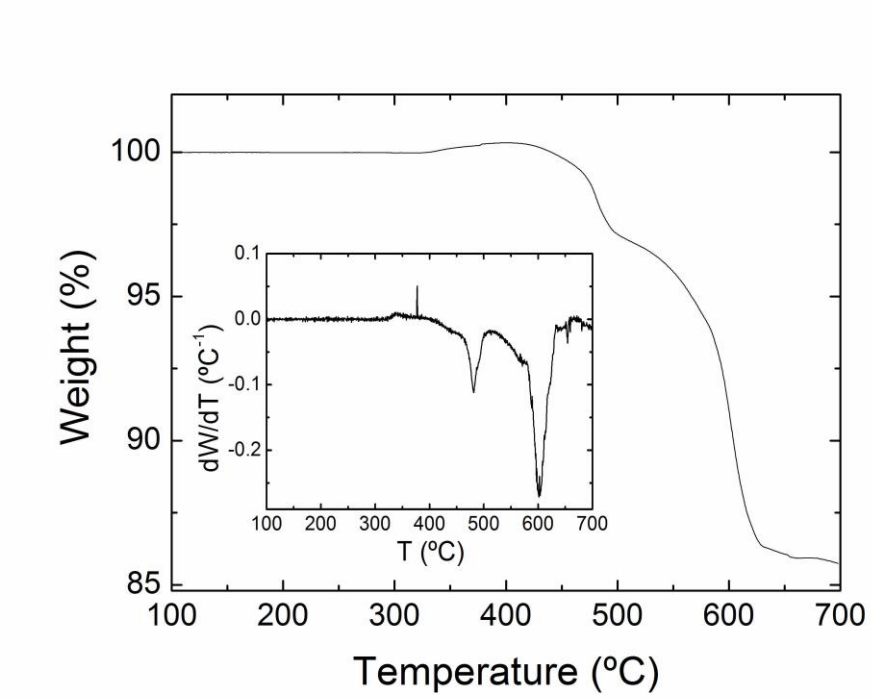

Figure 4

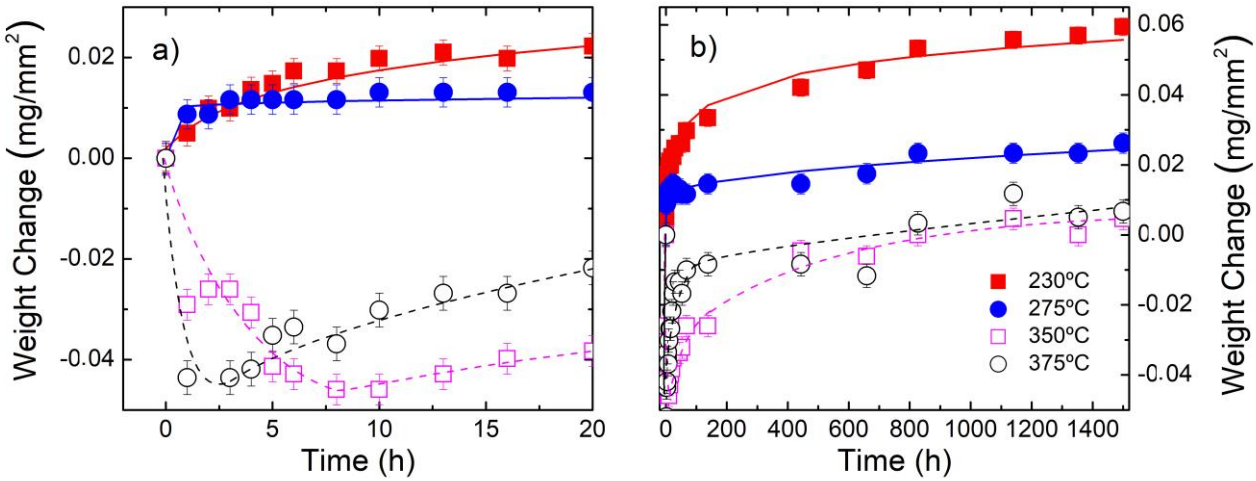

Figure 5

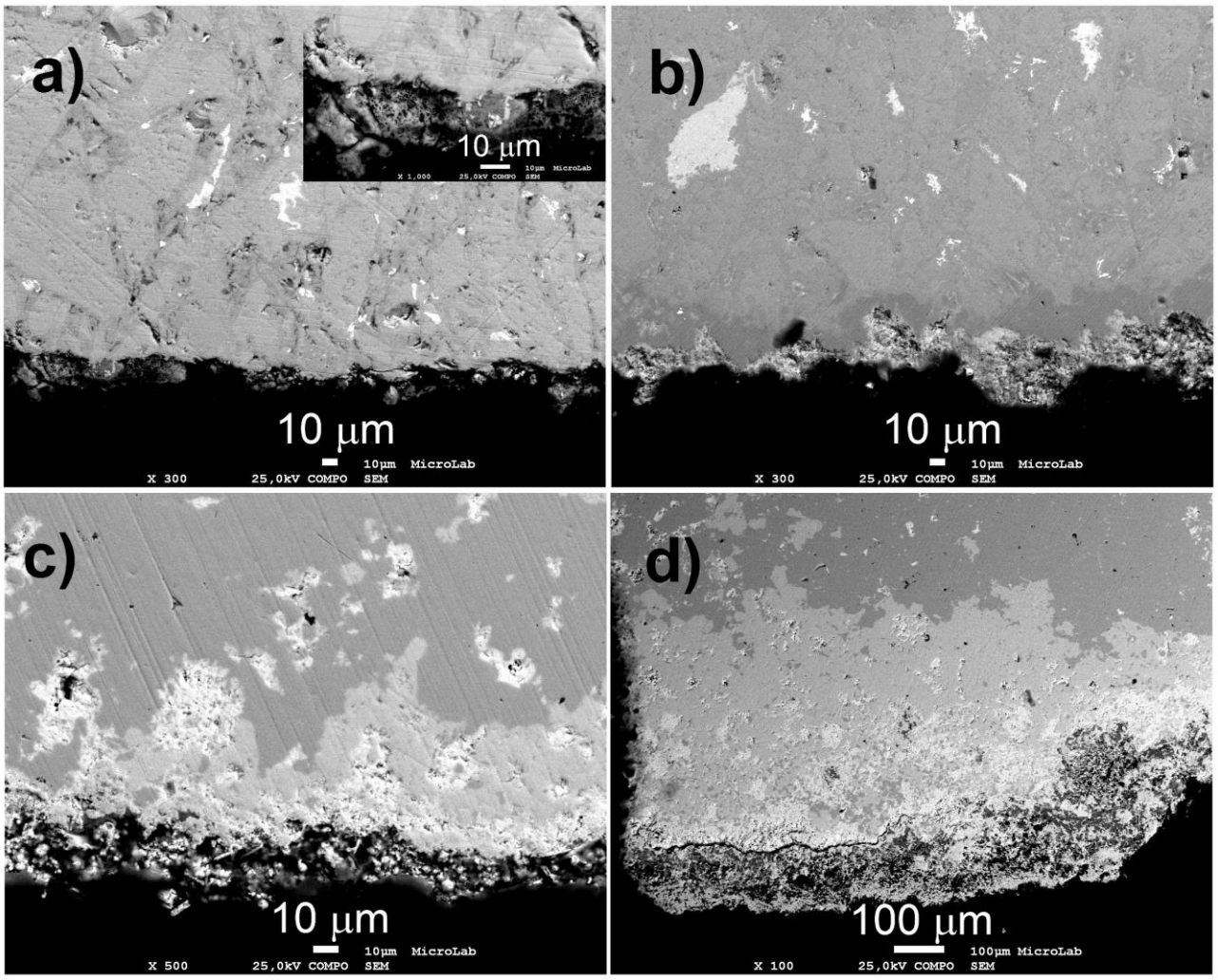
a)
10 µm
X 1,000 25,0kV COMPO SEM 10µm MicroLab
10 µm
X 300 25,0kV COMPO SEM 10µm MicroLab
b)
10 µm
X 300 25,0kV COMPO SEM 10µm MicroLab
c)
10 µm
X 500 25,0kV COMPO SEM 10µm MicroLab
d)
100 µm
X 100 25,0kV COMPO SEM 100µm MicroLab

Figure 6

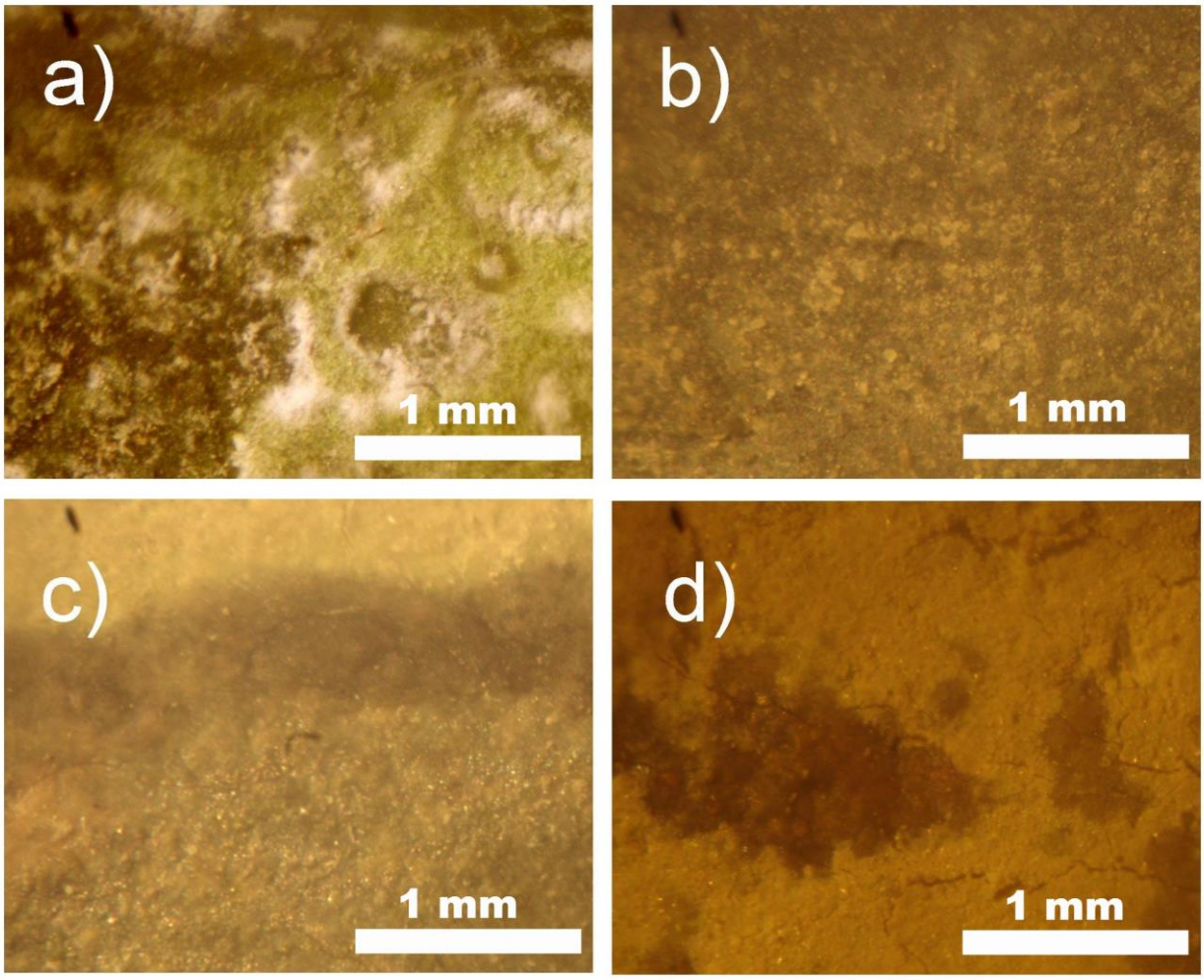

Figure 7

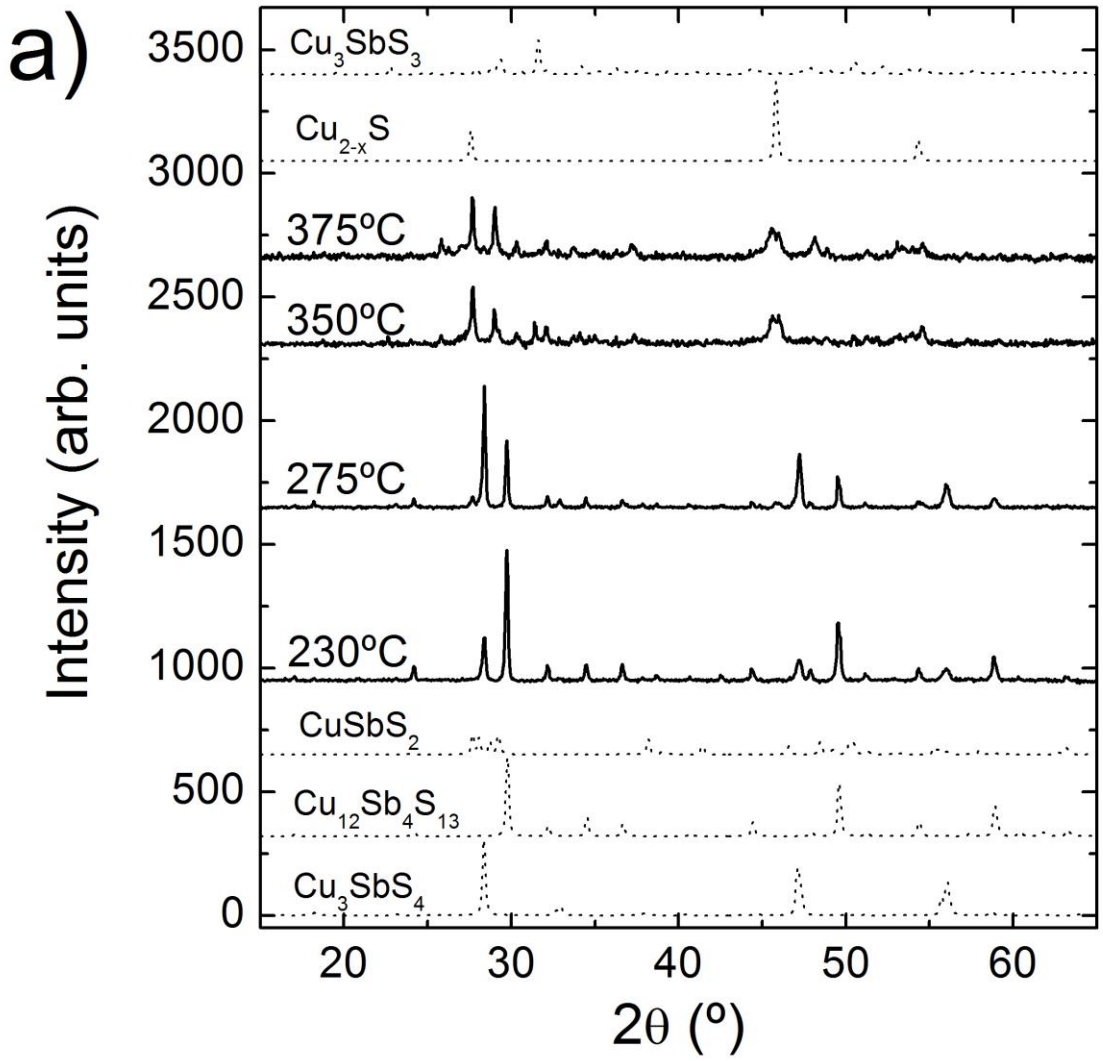
a)
Intensity (arb. units)
3500
3000
2500
2000
1500
1000
500
0
Cu3SbS3
Cu2-xS
375ºC
350ºC
275ºC
230ºC
CuSbS2
Cu12Sb4S13
Cu3SbS4
20
30
40
50
60
2θ (º)

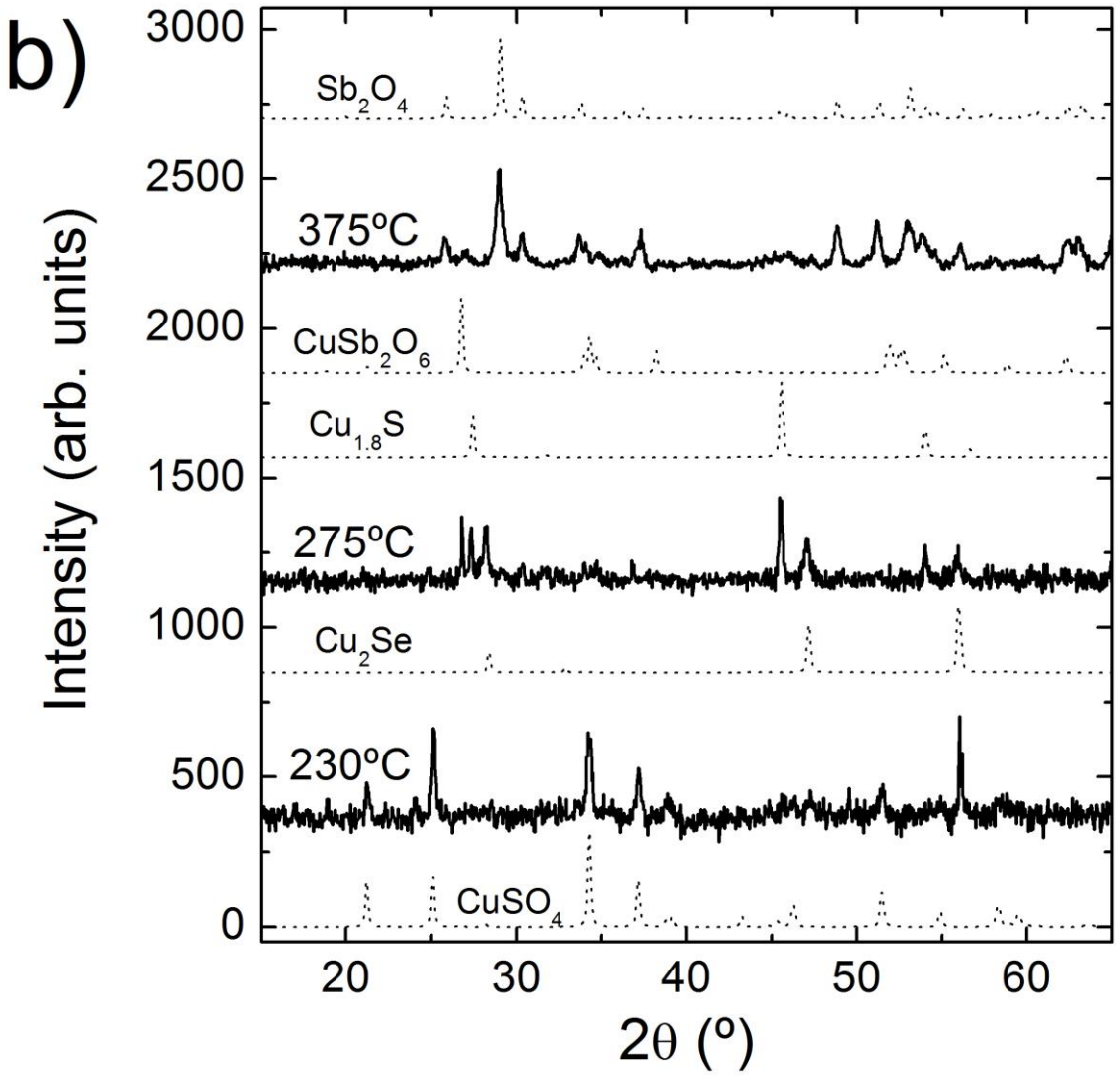
b)
Intensity (arb. units)
3000
2500
2000
1500
1000
500
0
Sb2O4
375ºC
CuSb2O6
Cu1.8S
275ºC
Cu2Se
230ºC
CuSO4
20
30
40
50
60
2θ (º)

Figure 8

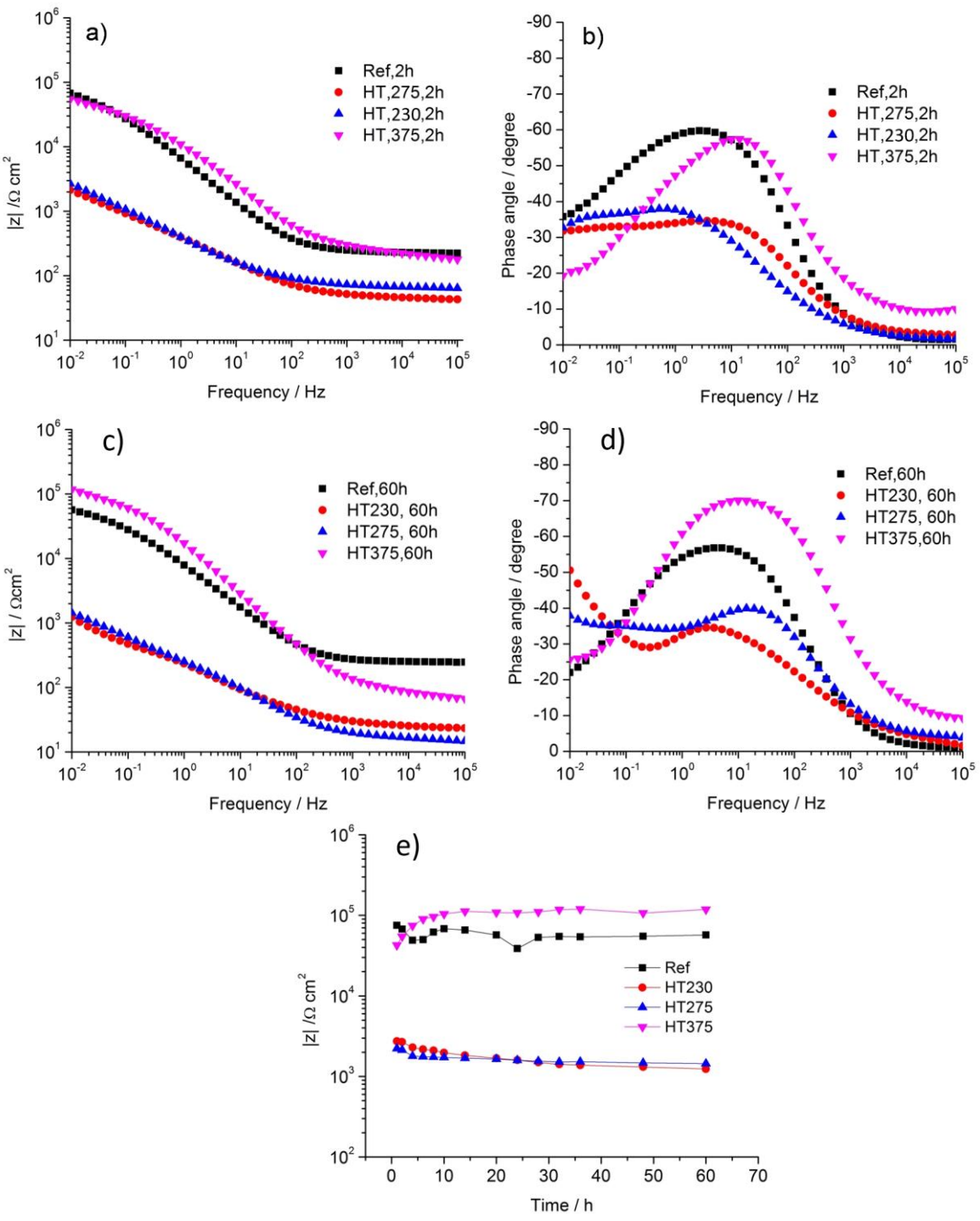
a)
Ref,2h
HT,275,2h
HT,230,2h
HT,375,2h
|z| /Ω cm²
Frequency / Hz
b)
Phase angle / degree
c)
Ref,60h
HT230, 60h
HT275, 60h
HT375,60h
|z| / Ωcm²
d)
e)
Ref
HT230
HT275
HT375
Time / h

Table I. Results from average EDS analysis for the phases in the Cu12Sb3.9Bi0.1S10Se3 oxidized samples.

Temperature (ºC)	**Region**	**Phase-type**	**Composition EDS / at. %**					
			Cu	**Sb**	**Bi**	**S**	**Se**	**O**
230	**Interior**	Grey: Cu12Sb4S13	42(1)	14(1)	-	36(1)	8(1)	-
		Dark grey: Cu3SbS4	51(4)	8(1)	-	21(3)	6(1)	14(5)
		White: CuSbS2	25(1)	22(1)	2(1)	17(1)	34(1)	-
	Surface	CuSO4	20(7)	-	-	1(1)	16(4)	64(3)
		Cu2Se	47(7)	-	-	-	35(6)	18(7)
275	**Interior**	Grey: Cu12Sb4S13	42(1)	14(1)	-	36(2)	9(2)	-
		Dark grey: Cu3SbS4	38(1)	13(1)	-	36(2)	13(1)	-
		Light grey: CuSbS2	29(2)	17(5)	3(2)	17(1)	34(2)	-
	Surface	Dark: Cu2-xS	65(2)	-	-	27(1)	8(1)	-
		Light: CuSb2O6	9(4)	27(4)	0(1)	6(2)	-	58(1)
350	**Interior**	Grey: Cu3SbS3	44(1)	14(1)	0(1)	31(2)	11(1)	-
		Dark grey: Cu2-xS	66(1)	-	-	25(1)	9(1)	-
	Surface	Grey: Cu3SbS3	45(2)	14(1)	0(1)	28(1)	13(1)	
		Light grey: CuSb2O6	8(2)	24(2)	0(1)	2(1)	-	66(2)
		Light: Sb2O4	1(1)	35(2)	-	-	-	64(2)
375	**Interior**	Grey: Cu3SbS3	44(2)	14(1)	-	29(1)	13(1)	-
		Dark grey: Cu2-xS	64(3)	3(3)	-	24(1)	9(1)	-
	Surface	Grey: Cu3SbS3	44(1)	14(1)	-	27(2)	15(2)	-
		Dark grey: Cu2-xS	65(1)	-	-	25(1)	10(1)	-
		Light: Sb2O4	6(3)	32(4)	0(1)	2(2)	-	60(4)